

Empirical and Simulated Performance Evaluation of Distributed Massive MIMO

David Löschenbrand, Markus Hofer, Benjamin Rainer, Thomas Zemen
Security & Communication Technologies, AIT Austrian Institute of Technology GmbH
 Vienna, Austria
 david.loeschenbrand@ait.ac.at

Abstract—We describe a distributed massive MIMO measurement campaign in an urban vehicular setting, where wireless channel measurements are acquired with two mobile stations equipped with a single antenna each and 32 antennas at the base station partitioned in two groups of 16 antennas each. We fit and assess various statistical distributions to characterize the observed propagation conditions and their dependency on time and space. Key parameters from the measurement are compared to simulations with a ray-tracing tool considering the geometry of the scenario. We evaluate distributed and collocated base station antenna setups in terms of singular value spread and achievable spectral efficiency for both measured and simulated channels and draw conclusions for optimal base station antenna placement.

Index Terms—distributed, massive MIMO, ray-tracing, measurement, sum-rate

I. INTRODUCTION

Besides increased data rates in the enhanced mobile broadband (eMBB) use-case, the new 5G standard also foresees novel applications like connected vehicles and industrial communications via its set of requirements for ultra-reliable low latency communication (URLLC). Achieving those requirements in safety critical scenarios asks for a deep understanding of the underlying wireless propagation conditions to ensure a proper physical layer design of the communication system.

Massive multiple-input multiple-output (MIMO) is widely considered as a suitable method to harness spatial diversity and eliminate small-scale fading, thus enabling URLLC. Since the near-optimality of linear processing techniques in massive MIMO systems depends on the propagation conditions in the wireless channel [1], distributed massive MIMO has gained much attention. It promises better separability of users (through uncorrelated channel realizations) and mitigation of large-scale fading [2]–[4]. Effects of varying base station antenna aperture sizes on the downlink sum spectral efficiency (SE) are reported in [5]. However, aforementioned work considers only analytical and numerical approaches based on channel models.

To validate the assumptions typically found in analytic papers, actual channel measurements are of utmost importance. They are in turn used to parametrize channel models such that they correctly reproduce real world propagation effects.

Contribution of this paper:

- We describe a measurement campaign conducted with the AIT massive MIMO channel sounder in a highly dynamic

vehicle-to-infrastructure (V2I) setting with distributed and collocated antenna array configurations.

- We introduce the AIT ray tracing (RT) tool that is able to reproduce the empirical data in a spatially consistent manner.
- We analyze statistical properties as well as the Rician K -factor and singular value spread (SVS) distribution over space with distributed and collocated antenna array configurations, both with empiric and simulated data.

II. SIGNAL MODEL

We consider the massive MIMO uplink case, where the number of receive antennas M is far greater than the number of transmit antennas K , i.e. $M \gg K \geq 1$. The vector $\mathbf{x}_{qs} = [x_{qs}^1, \dots, x_{qs}^K]^T$ groups the signals x_{qs}^k of the k -th transmitter (similarly, $\mathbf{y}_{qs} = [y_{qs}^1, \dots, y_{qs}^M]^T$ for the receiver), the subcarrier index is denoted by q and the time index by s . The time- and frequency variant MIMO uplink signal model reads

$$\mathbf{y}_{qs} = \mathbf{H}_{qs}\mathbf{x}_{qs} + \mathbf{z}_{qs}. \quad (1)$$

The channel matrix $\mathbf{H}_{qs} = [\mathbf{h}_{qs}^1, \dots, \mathbf{h}_{qs}^K] \in \mathbb{C}^{M \times K}$ contains the channel vectors $\mathbf{h}_{qs}^k = [h_{qs}^{1k}, \dots, h_{qs}^{Mk}]^T$ from transmitter k to all M receivers. The noise \mathbf{z}_{qs} is considered i.i.d. random complex Gaussian.

Since we aim to compare empirical and simulated channel data, an estimate for the channel matrix \mathbf{H}_{qs} of the urban scenario is obtained in two different ways. The first method is to use data obtained during measurements and perform point wise division of the received symbols $\hat{\mathbf{y}}_{qs}$ with the transmitted symbols \mathbf{x}_{qs} (already corrected for impairments of the radio frequency (RF) hardware)

$$\hat{\mathbf{H}}_{qs} = \frac{\hat{\mathbf{y}}_{qs}}{\mathbf{x}_{qs}}. \quad (2)$$

The second method estimates the channel matrix by using parameters obtained with the AIT RT tool. It is derived by superposition of P_s RT paths p with the respective complex attenuation η_{sp}^{mk} and delay τ_{sp}^{mk} . The (m, k) -th element of the channel matrix is given by

$$(\tilde{\mathbf{H}}_{qs})_{m,k} = h_q^{\text{TX}} h_q^{\text{RX}} \sum_{p=1}^{P_s} \eta_{sp}^{mk} e^{-j2\pi(\tau_{sp}^{mk}(f_c - B/2 + q\Delta f))}. \quad (3)$$

The expressions h_q^{TX} and h_q^{RX} denote the band limiting transmit and receive filters, respectively.

The sampled finite bandwidth channel impulse response (CIR) for both methods and antenna pair (m, k) is calculated via the inverse Fourier transform over the bandwidth $B = Q\Delta f$

$$g_{ns}^{mk} = \frac{1}{Q} \sum_{q=0}^{Q-1} h_{qs}^{mk} e^{j2\pi nq/Q}, \quad (4)$$

with n being the delay index.

The channel sounder measurements are performed with a bandwidth of 115 MHz and the RT tool in itself is not band limited. For the analysis in the next chapter, we choose a bandwidth $B = 20$ MHz. To fit with the tone spacing $\Delta f = 240$ kHz of the measurement, we choose the same value also for the RT. The time index is chosen as a multiple of the channel sounder repetition rate, i.e. absolute time $t = sT_{\text{rep}}$. Since the time variability in our setup mainly arises through the movement of the transmitter and there is detailed geometrical knowledge of the scenario available (position and velocity through global navigation satellite system (GNSS) tracking for the measurements and the geometrical model for RT), we assume a one-to-one mapping of time to spatial position of the transmit antennas. Therefore, s and $\mathbf{s} = [s_x, s_y, s_z]^T$ denoting time and space, respectively, will be used interchangeably in the following sections.

A. Stochastic Characterization

Commonly, Rayleigh fading is assumed in the massive MIMO literature to achieve favorable propagation conditions and harness the full potential of the vast amount of antennas. However, this assumption is under many real propagation circumstances not legitimate and we instead observe Rician fading with a dominant path.

To determine the fading characteristics of the measured scenario, we analyze the stochastic distribution of the signal envelope over time/space. This is done by considering the first strong delay bin of the CIR in (4), i.e. the distribution of the set $\mathcal{G} = \{\max_n |g_{ns}^{mk}|\}$, for (m, k, s) in a given parameter set defined in (5). The first strong delay component critically determines the performance of communication systems based on correlation synchronization such as orthogonal frequency-division multiplexing (OFDM) [6]. Large-scale fading effects on the envelope's distribution are avoided by normalizing the signal with its mean power over a sliding time window of length 600 ms [6]. This guarantees that only small-scale fading determines power variations within the elements of \mathcal{G} . To obtain enough small-scale fading realizations, we assume stationarity over a time interval $T_{\text{stat}} = 500$ ms (equivalent to at most 7 m $\approx 82\lambda$ with a maximum speed in our scenario of 13.9 m/s) and use all obtained samples within this time frame. Further, since closely spaced antennas also receive different realizations of the same random fading process, we allow for more than one receive and transmit index.

Therefore, the set \mathcal{G} is constituted of elements chosen from discrete intervals

$$\mathcal{G} = \left\{ \max_n |g_{ns}^{mk}| : m \in \bar{m}, k \in \bar{k}, s \in \bar{s} \right\} \quad (5)$$

with $\bar{m} \subseteq [1, M]$, $\bar{k} \subseteq [1, K]$ and $\bar{s} \subseteq [s_0, s_0 + T_{\text{stat}})$.

Fitting of the empirical and simulated envelope distribution \mathcal{G} to several well known probability distributions is performed with the proprietary *Statistics and Machine Learning Toolbox* of Matlab. The Kolmogorov-Smirnov (KS) criterion [7]

$$\text{GoF} = \sup_z |F_Z(z) - F_G(z)| \quad (6)$$

is used to assess the goodness of fit (GoF) of an empirical cumulative distribution function (CDF) $F_G(z)$ to its analytical counterpart $F_Z(z)$ [6]. A good fit is indicated by a small value of GoF.

B. Channel Orthogonality

The (near-) orthogonality of channel vectors \mathbf{h}_{qs}^k and $\mathbf{h}_{qs}^{k'}$, i.e. $\mathbf{h}_{qs}^k \mathbf{h}_{qs}^{k'} \approx 0$ for $k \neq k'$ is of crucial importance for the performance of linear beam forming like maximum ratio combining (MRC) and minimum mean square error (MMSE) techniques as it determines the signal-to-interference-and-noise ratio (SINR), see (9). To quantize the orthogonality of the channel vectors, we revert to the SVS defined as the ratio

$$\gamma(\mathbf{H}_{qs}) = \frac{\sigma_{qs}^{k_{\text{max}}}}{\sigma_{qs}^{k_{\text{min}}}} \quad (7)$$

of largest to smallest singular value of the channel matrix.

The singular values are defined by decomposing the channel matrix

$$\mathbf{H}_{qs} = \mathbf{U}_{qs} \mathbf{\Sigma}_{qs} \mathbf{V}_{qs}^H \quad (8)$$

into unitary matrices $\mathbf{U}_{qs} \in \mathbb{C}^{M \times M}$, $\mathbf{V}_{qs} \in \mathbb{C}^{K \times K}$, and the rectangular matrix $\mathbf{\Sigma}_{qs} \in \mathbb{C}^{M \times K}$ with K singular values σ_{qs}^k on its main diagonal.

A small SVS indicates that the channel vectors reside in orthogonal eigenspaces whereas a large value of the SVS indicates their linear dependency. With orthogonal channel vectors and through the law of large numbers, small scale fading is eliminated - a favorable effect called channel hardening [8].

Given K users with equal and unit transmit power and MRC at the receiver, the ergodic achievable SE for user k reads as [9]

$$\text{SE}^k = \mathbb{E} \left\{ \log_2 \left(1 + \frac{|\mathbf{h}_{qs}^k \mathbf{h}_{qs}^k|^2}{\sum_{k'=1, k' \neq k}^K |\mathbf{h}_{qs}^k \mathbf{h}_{qs}^{k'}|^2 + \|\mathbf{h}_{qs}^k\|^2} \right) \right\}. \quad (9)$$

We assume an ergodic channel and denote the expectation with $\mathbb{E}\{\cdot\}$. The achievable ergodic sum SE is then defined as the sum of the individual SEs,

$$\text{SE} = \sum_{k=1}^K \text{SE}^k. \quad (10)$$

III. SCENARIO DESCRIPTION FOR MEASUREMENTS AND MODELING

A. Measurement Scenario

We conducted distributed massive MIMO V2I measurements in an urban environment around the AIT's office premises (48.269 080°N, 16.427 637°E).

The receiver RX of the AIT massive MIMO channel sounder [10] is positioned on top of an office building at

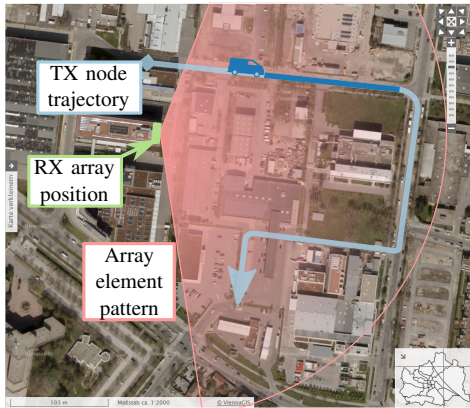


Fig. 1. Birdview of the urban measurement scenario in Vienna. The full trajectory of the TX node carrying TX 1 and TX 2 is indicated in light blue and the trajectory part of interest in dark blue. The position of the RX array on top of the office building (both for collocated and distributed setup) is indicated in light green, and the visibility region for the RX antenna array elements is indicated in light red.

approximately 25 m height. It features 32 parallel receive ports grouped into two antenna arrays with 16 dual polarized patch antenna elements each. With these two receive antenna arrays, a *collocated* (antenna arrays next to each other with 0.5 m distance) and a *distributed* (antenna arrays with 7.5 m distance) setup is realized. For both setups, the antenna arrays are facing in the same direction (east, see Figure 1).

Two transmitters TX 1 and TX 2 are mounted into one car (referred to as *TX node*) with their respective omnidirectional monopole antennas being placed on the car's roof with a distance of 1 m. The TX node follows a fixed trajectory on a two way street with light traffic through an urban scenario with vegetation, parking cars, metallic construction site objects and factory halls. The maximum speed of the TX node is approximately 50 km/h (13.9 m/s). The position of the car is recorded via GNSSs and mapped to the obtained channel measurements. For each receive antenna array setup, ten measurement runs are conducted to gain statistical significance.

Figure 1 shows the measurement scenario with the TX node trajectory (carrying TX 1 and TX 2), the RX antenna array position on top of the office building and the direction of the array element beam pattern, facing east. The detailed channel sounding parameters can be found in [10].

B. Ray Tracing Implementation

To analyze the measurement scenario in more detail without the need for new measurements, we derive a detailed and spatially consistent RT model. This allows us to evaluate varying array geometries in different environments in future work. We implement the AIT RT using the NVIDIA Optix RT engine. We follow a hybrid approach, where in a first step possible reflection, diffraction, and diffuse scattering points on surfaces are identified without rigorous validity checks with the 3D geometric model depicted in Fig. 2. In the second step, we launch rays towards these points in space using NVIDIA Optix. We support and implement the following mechanisms for identifying reflections, diffractions, and diffuse scattering points and computing their corresponding electromagnetic field:

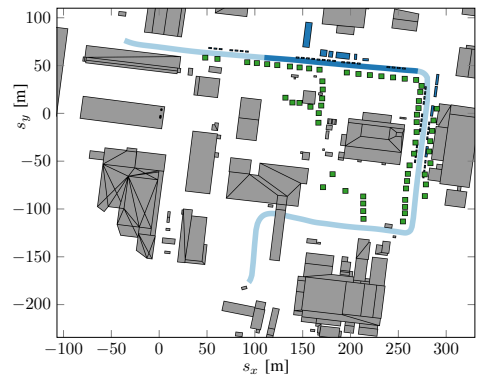


Fig. 2. RT 3D model including buildings (grey), vegetation (green) and metallic structures (blue) derived from openly available building data bases. The TX node trajectory as recorded during measurements is indicated in light blue and the trajectory of interest in this paper is indicated in dark blue.

- 1) l -th order specular reflections by the image method (Snell's law);
- 2) Edge diffraction according to the uniform theory of diffraction (UTD) [11];
- 3) Points on surfaces for diffuse tiling according to [12], [13] and a novel tiling method based on lattices including the Lambertian and directive scattering model [14].

In this paper we use the directive scattering model and lattice-based¹ tiling in order to obtain a correlated Doppler spectral density. The basis for the tiling of surfaces is select as

$$\mathbf{b}_i = \frac{\mathbf{u}_i}{\|\mathbf{u}_i\|_2} \frac{c}{2B}, \quad i \in \{1, 2\} \quad (11)$$

where \mathbf{u}_i is the i -th spanning vector of a surface, B the system bandwidth (in this paper 115.44 MHz) and c denotes the speed of light. This leads to the fact that each first order diffuse scattering ray falls into a different delay bin. We implement higher order diffuse scattering by tracing the specular reflection of each diffuse scattering point.

To the best of the authors knowledge, this is the first implementation capable of reproducing measured Doppler spectra over time with diffuse scattering through spatially consistent RT.

IV. EMPIRICAL AND SIMULATED RESULTS

To analyze the time-variant characteristics of (4) for both measurements and RT, we revert to the time-variant power delay profile (PDP) and the time-variant Doppler spectral density (DSD). They are obtained as marginals of the local scattering function (LSF) (see [15], [16] for more details).

Figure 3 shows the PDP and DSD of one segment of the TX node trajectory ($s_x \in [115 \text{ m}, 270 \text{ m}]$), which constitutes our region of interest for this paper. Qualitatively, we observe a good match between measurements and RT results. In the PDP, the line of sight (LOS) shows the same temporal characteristics, although the power level fluctuation due to vegetation next to the street is less pronounced with RT. The delay distribution of diffuse scattering over time is well captured in the simulation. The DSD shows the same strong

¹A lattice Λ^n is defined as a subgroup of \mathbb{R}^n as $\Lambda^n(\mathbf{b}_1, \dots, \mathbf{b}_n) := \{\sum_{i=1}^n \alpha_i \mathbf{b}_i : \alpha_i \in \mathbb{Z}\}$, where $\{\mathbf{b}_1, \dots, \mathbf{b}_n\} \subset \mathbb{R}^n$ is a basis.

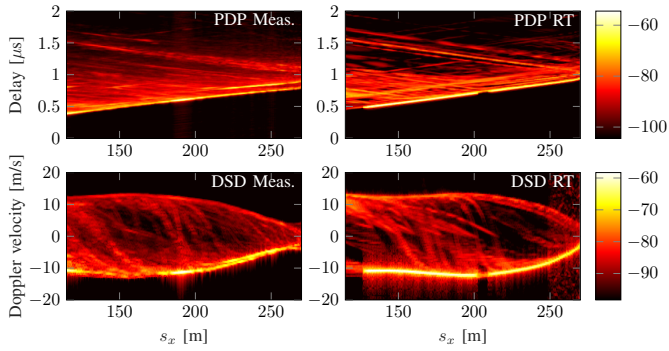


Fig. 3. Comparison of measured and simulated PDP and DSD over TX node position.

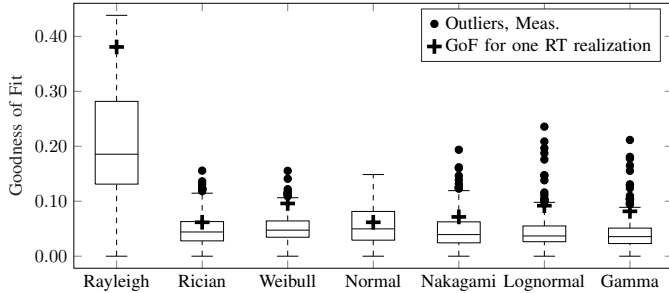


Fig. 4. Box plot of the GoF for several probability distributions. The boxes span the 25 – 75 percentile and the horizontal line in the box shows the median GoF. The length of the whiskers is at most 1.5 times the box height (covering 99% of a normal distribution) and outliers are marked as dots.

LOS path without much large-scale fading due to vegetation with the RT. Again, the changing Doppler frequencies over time of the diffuse scattering reproduce the measurement data very well.

A. Stochastic Evaluation

To analyze which probability distribution fits the measurement data best, we choose the realization set \mathcal{G} from (5) with $\bar{m} = [1, 16]$, $\bar{k} = 1$ and $\bar{s} = [s_0, s_0 + T_{\text{stat}}]$ and fit the well known Rayleigh and Rice distribution as well as other common probability distributions. The time index s_0 is varied to obtain several fits along the trajectory of interest, i.e. s_0 chosen such that $s_x \in [115 \text{ m}, 270 \text{ m}]$, $s_y > 40 \text{ m}$.

Given the shape parameters w and ν of a Rician distributions for the realization set \mathcal{G} , the Rician K -factor describing the power ratio of the LOS path to all other multipath contributions is defined as $\kappa(\mathcal{G}) = \nu^2/2w^2$.

Figure 4 shows the box plot of the GoF (6) for all fitted distributions to the measurement data along the TX node trajectory. Clearly, the assumption of Rayleigh fading is not valid in our scenario. Assuming Rician fading, we observe a good fit (low GoF) with low median (horizontal line in the box) and few outliers (dots above the whiskers). Other probability distributions do not provide a significantly better GoF and are therefore not considered further.

For every Rician distribution fit along the TX trajectory, we evaluate the Rician K -factor $\kappa(\mathcal{G})$ to analyze its spatial dependencies and characteristics. Further, we perform two separate fits for each of the RX antenna arrays, i.e. for $m \in [1, 16]$ and $m \in [17, 32]$. The top plot in Fig. 5 shows $\kappa(\mathcal{G})$ for the first (blue) and second (red) RX array for the

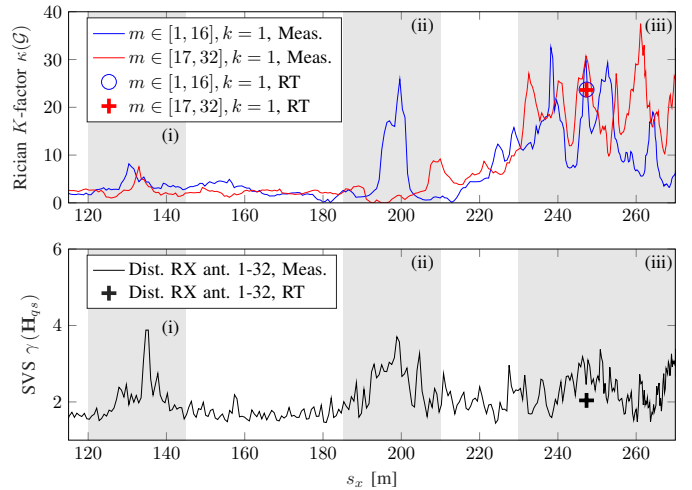


Fig. 5. Rician K -factor $\kappa(\mathcal{G})$ (top) and SVS $\gamma(\mathbf{H}_{qs})$ (bottom) over TX node position from measured and simulated data for the distributed RX setup.

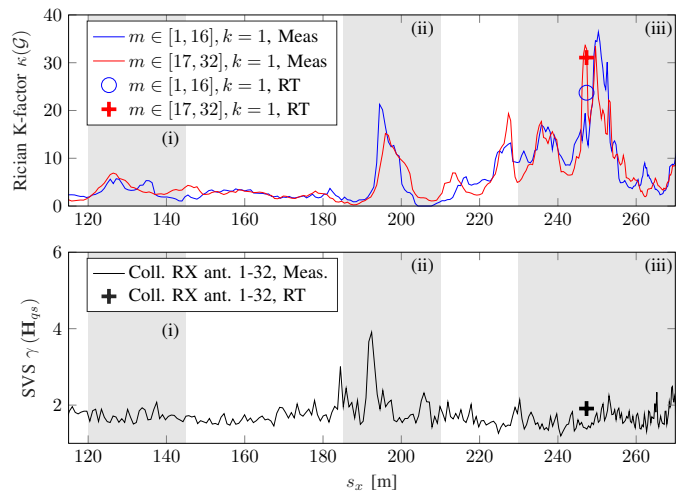


Fig. 6. Rician K -factor $\kappa(\mathcal{G})$ (top) and SVS $\gamma(\mathbf{H}_{qs})$ (bottom) over TX node position from measured and simulated data for the collocated RX setup.

distributed RX setup. We observe three regions (i)-(iii) with increased LOS contributions. In region (ii) only the first RX array exhibits LOS propagation conditions whereas the K -factor for the second array stays low.

The top plot in Fig. 6 shows $\kappa(\mathcal{G})$ for the first (blue) and second (red) RX array for the collocated RX setup. Again, we observe three regions (i)-(iii) with increased LOS contributions. In region (ii), given the proximity of the RX arrays, both of them exhibit high K -factors.

B. Channel Orthogonality Evaluation

The SVS is calculated for the full measured channel matrix $\hat{\mathbf{H}}_{qs} \in \mathbb{C}^{M \times K}$ at every position \mathbf{s} along the TX node trajectory of interest according to (7). The mean of 50 consecutive SVS values $1/50 \sum_{s=s_0}^{s_0+49} \gamma(\hat{\mathbf{H}}_{qs}[q, s])$ is then plotted over the position \mathbf{s} associated with $s_0 + 25$.

The bottom plot of Fig. 5 shows the SVS $\gamma(\hat{\mathbf{H}}_{qs})$ over position for the distributed RX antenna setup. We observe three regions (i)-(iii) with increased SVS and therefore decreased orthogonality between the channel vectors \mathbf{h}_{qs}^1 and \mathbf{h}_{qs}^2 (see section II-B). The three regions coincide with the strong LOS occurrences identified with the Rician K -factor.

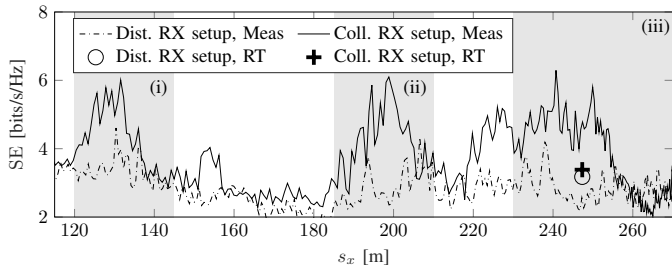


Fig. 7. Ergodic achievable uplink sum SE over TX node position for a mean SNR of 6 dB. In LOS propagation conditions, the collocated RX setup achieves higher sum SEs.

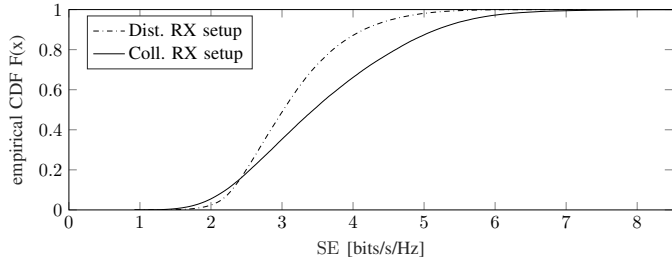


Fig. 8. Empirical CDF of the ergodic achievable uplink sum SE for realizations over the TX node trajectory from 6 measurement runs.

The bottom plot of Fig. 6 shows the SVS $\gamma(\hat{\mathbf{H}}_{qs})$ over the position for the collocated RX antenna setup. We observe only one region (ii) with increased SVS whereas regions (i) and (iii) show low SVS values despite high K -factors. Therefore, in terms of the SVS, the collocated RX setup is the preferred one in this particular scenario.

The orthogonality of the channel vectors directly impacts the SINR and therefore the achievable uplink sum SE, see (10). In Fig. 7 we show a comparison of the sum SE for the distributed and collocated RX setup. For this, the instantaneous sum SE is calculated according to (10) for every position along the TX trajectory and afterwards the mean over 50 consecutive positions is obtained. The mean signal-to-noise ratio (SNR) over all positions under consideration is normalized to be 6 dB. In the plot, we clearly observe high SE in the LOS regions (i)-(iii) for the collocated RX setup, meaning that this setup can harvest the high received power of the LOS while keeping the SINR low. For the distributed setup, the aforementioned effects cancel each other out, resulting in a more or less constant sum SE below the level of the collocated setup.

To avoid coincidental results, we performed the sum SE analysis over 6 TX node trajectory runs for both the distributed and collocated RX setup. Fig. 8 shows the empirical CDF of the ergodic achievable uplink sum SE for this analysis. Again, the collocated RX setup shows clear performance benefits with a higher achievable sum SE on average.

V. CONCLUSION

In this paper, we have presented an urban vehicular massive MIMO measurement campaign with collocated and distributed antenna array configurations. We showed that a Rician fading model is applicable and describes the statistical properties of the measurement well. By investigating the spatial dependencies of the Rician K -factor and the SVS, we found that in our LOS scenario, the collocated setup performs better than

the distributed setup in terms of SE. We suspect the cause to be different large scale fading realizations for the two antenna arrays causing an imbalance in the received signal magnitude, thereby effectively cutting the number of significant antennas in half and increasing the channel vector correlation. Further, we introduced the AIT RT tool that accurately reproduces the temporal and statistical characteristics of the measurement data.

ACKNOWLEDGMENT

This work is funded by the Austrian Research Promotion Agency (FFG) and the Austrian Ministry for Transport, Innovation and Technology (bmvit) within the project MARCONI (861208) of the funding program ICT of the Future.

REFERENCES

- [1] T. L. Marzetta, "Noncooperative cellular wireless with unlimited numbers of base station antennas," *IEEE Transactions on Wireless Communications*, vol. 9, no. 11, pp. 3590–3600, 2010.
- [2] J. Li, D. Wang, P. Zhu, and X. You, "Uplink Spectral Efficiency Analysis of Distributed Massive MIMO with Channel Impairments," *IEEE Access*, vol. 5, pp. 5020–5030, 2017.
- [3] G. N. Kamga, M. Xia, and S. Aissa, "Spectral-Efficiency Analysis of Massive MIMO Systems in Centralized and Distributed Schemes," *IEEE Transactions on Communications*, vol. 64, no. 5, pp. 1930–1941, 2016.
- [4] K. T. Truong and R. W. Heath, "The viability of distributed antennas for massive MIMO systems," in *Asilomar Conference on Signals, Systems and Computers*, 2013, pp. 1318–1323.
- [5] S. Pratschner, E. Zöchmann, H. Groll, S. Caban, S. Schwarz, and M. Rupp, "Does a Large Array Aperture Pay Off in Line-Of-Sight Massive MIMO?" in *2019 IEEE 20th International Workshop on Signal Processing Advances in Wireless Communications (SPAWC)*, 2019, pp. 1–5.
- [6] L. Bernadó, T. Zemen, F. Tufvesson, A. F. Molisch, and C. F. Mecklenbräuer, "Time- and Frequency-Varying K -Factor of Non-Stationary Vehicular Channels for Safety Relevant Scenarios," *IEEE Transactions on Intelligent Transportation Systems*, vol. 16, no. 2, pp. 1007–1017, 2015.
- [7] F. J. Massey Jr., "The Kolmogorov-Smirnov Test for Goodness of Fit," *Journal of the American Statistical Association*, vol. 46, no. 253, pp. 68–78, 1951.
- [8] T. Zemen, D. Löschenbrand, M. Hofer, C. Pacher, and B. Rainer, "Orthogonally Precoded Massive MIMO for High Mobility Scenarios," *IEEE Access*, vol. 7, pp. 132979–132990, 2019.
- [9] H. Q. Ngo, E. G. Larsson, and T. L. Marzetta, "Energy and spectral efficiency of very large multiuser MIMO systems," *IEEE Transactions on Communications*, vol. 61, no. 4, pp. 1436–1449, 2013.
- [10] D. Löschenbrand, M. Hofer, L. Bernadó, G. Humer, B. Schrenk, S. Zelenbaba, and T. Zemen, "Distributed Massive MIMO Channel Measurements in Urban Vehicular Scenario," in *13th European Conference on Antennas and Propagation (EuCAP)*, 2019, pp. 1–5.
- [11] R. G. Kouyoumjian and P. H. Pathak, "A uniform geometrical theory of diffraction for an edge in a perfectly conducting surface," *Proceedings of the IEEE*, vol. 62, no. 11, pp. 1448–1461, Nov 1974.
- [12] F. Mani, F. Quitin, and C. Oestges, "Accuracy of depolarization and delay spread predictions using advanced ray-based modeling in indoor scenarios," *EURASIP Journal on Wireless Communications and Networking*, vol. 2011, no. 1, p. 11, Jun 2011.
- [13] M. Gan, X. Li, F. Tufvesson, and T. Zemen, "An effective subdivision algorithm for diffuse scattering of ray tracing," in *2014 XXXIth URSI General Assembly and Scientific Symposium (URSI GASS)*, Aug 2014, pp. 1–4.
- [14] V. Degli-Esposti, F. Fuschini, E. M. Vitucci, and G. Falciasecca, "Measurement and modelling of scattering from buildings," *IEEE Transactions on Antennas and Propagation*, vol. 55, no. 1, pp. 143–153, Jan 2007.
- [15] L. Bernadó, T. Zemen, F. Tufvesson, A. F. Molisch, and C. F. Mecklenbräuer, "Delay and Doppler Spreads of Non-Stationary Vehicular Channels for Safety Relevant Scenarios," *IEEE Transactions on Vehicular Technology*, vol. 63, no. 1, pp. 82–93, 2014.
- [16] G. Matz, "On non-WSSUS wireless fading channels," *IEEE Transactions on Wireless Communications*, vol. 4, no. 5, pp. 2465–2478, 2005.